3D INSTRUMENT SELF-SHADING EFFECTS ON IN–WATER MULTI-DIRECTIONAL RADIANCE MEASUREMENTS

John P. Doyle, Department of Physics, Imperial College, University of London, UK
Kenneth J. Voss, Department of Physics, University of Miami, Coral Gables, USA

INTRODUCTION

It has been shown, in a theoretical work by Morel and Gentili (1993), that the upward radiance field just beneath, and just above, the ocean surface is in most cases not isotropic. This anisotropy results mainly from the nonisotropic characteristics of the water body's volume scattering function, combined with the lighting conditions that exist above the ocean surface: the sun's position and the relative proportions of direct and diffuse illumination. The theoretical anisotropy found in the upwelled radiance field structure has been substantiated by a comparison (Morel, Voss and Gentili 1995) with field measurements operated at sea using a submersible radiance distribution camera system (RADS), developed by Voss (1989). The RADS instrument is based on two electro-optic cameras, each one equipped with a fish-eye lens, enabling the complete (down- and upwelling) radiance distribution to be simultaneously captured at various depths and wavelengths. In the present work only the upwelling radiance hemisphere is addressed.

As reported in the quoted work by Morel, Voss and Gentili, one difficulty encountered in interpreting the marine signal produced by the RADS instrument is connected with an anomalously dark zone recorded in the antisolar plane, not exactly centered with respect to the antisolar direction. This dark zone presents a peak centered along a direction pointing higher up than the antisolar point (Gordon, personal communication). This anomaly, stronger at longer wavelengths, has been attributed to some vestige of an instrument self-shadowing effect.

This paper investigates this hypothesis, substantiating it with Monte Carlo computations. The solar radiation transport within the three-dimensional (3D) sun-ocean-atmosphere-RADS system is simulated making use of a fully 3D, backward Monte Carlo code (PHOTRAN). This code has been developed and tested by one of the authors (Doyle and Rief 1998, Doyle 2000) and, in its recently implemented extended version (PHOTRACK), permits quadratic surfaces to be fully included in the geometry description of the simulated system. This allows, for instance, imbedding the cylindrically shaped RADS instrument casing within an otherwise plane-parallel ocean-atmosphere system. Simulations can then be carried out, as further documented in this work, to demonstrate the previously noted "anomalous" RADS shadowing features, and show moreover that the shadowing peak is asymmetric with respect to the maximum shadowing direction.

The theoretical work presented in this paper is aimed at quantifying—as a function of the most relevant environmental, optical, and geometrical parameters—the RADS self-shading perturbations induced in the measured upwelled radiance field. Simulations provide the directional radiance percentage error with respect to a non-shadowed signal, at four different active sensor locations on the RADS lower surface. In addition comparison with a bi-dimensional—i.e. flat—disk-like instrument is also provided, and considerations on the conventional shadow-correction scheme operated on radiance and integrated radiance measurements are also given.

SUN-ATMOSPHERE-OCEAN-RADS SYSTEM

The general sun-atmosphere-ocean-RADS system adopted within the simulations is described as follows. Monochromatic solar radiation in the visible range, of given wavelength λ (no bandwidth integration is performed), and of incoming top of the atmosphere irradiance E_0, is tracked all the way to (in fact, backtracked from) the instrument sensors. E_0 is taken from Neckel and Labs (1984) allowing if needed for mean sun-earth distance, but for the purposes of this work, E_0 may be assumed unitary since absolute radiometric quantities are not required. Collimated radiation impinges on the top of the atmosphere with solar zenith angle θ_0, measured from the vertically upward direction. Three atmospheric optically active components are considered: ozone, air molecules, and aerosols. τ_{ozo} is the purely absorbing ozone optical depth (ood), the only absorbing atmospheric component considered here; it relates to a given load of ozone, expressed in Dobson units (DU) across the atmospheric column, through ozone specific absorption coefficients taken from Vigroux (1953). τ_{mol} is the purely scattering molecular optical depth (mod), undergoing Rayleigh scattering, and is a function of the given atmospheric pressure at sea level (Frölich and Shaw 1980, Young 1980). τ_{aer} is the purely scattering aerosol optical depth (aod), scattering according to a given aerosol phase function phfn_{aer} of the two-term Henyey-Greenstein (TTHG) type. The three atmospheric components are assumed uniformly distributed over a plane-parallel atmospheric layer extending 60 km above sea level, with refractive index $n_{atm} = 1.000$.

The air-sea interface is here assumed flat, above an infinitely deep (photons travelling beyond 10,000 km depth are lost) oceanic plane-parallel layer of refractive index $n_{oce} = 1.341$. Within it two oceanic components are considered as optically active: the water itself, and the particulate matter suspended (and dissolved) within. Water is characterized by Einstein-Smoluchowsky scattering through a phase function given in Morel and Gentili (1991) (it includes a less than unitary polarization factor), and by pure water absorption coefficient a_w (Pope and Fry 1997) and scattering coefficient b_w (Buiteveldt, Hakvoort and Donze 1994). Suspended in–water particulate matter scatters according to a given particulate phase function phfn_p of the tabulated type, and is assigned absorption coefficient a_p and scattering coefficient b_p, with corresponding particulate attenuation coefficient $c_p = a_p + b_p$ and particulate single scattering albedo $\omega_{0p} = b_p / c_p$.

A 3D cylinder, with a circular base and a vertical symmetry axis, measuring 50 cm in height and 20 cm in radius describes the RADS instrument. The RADS casing is assumed perfectly absorbing (i.e., black), and the simulated sensors are point-detectors located on its lower flat circular face. Two cases are considered: a totally flat (i.e., disk-like) RADS, and a fully vertically-extended 3D RADS instrument. Sensors are located *i)* centrally on the symmetry axis (for both flat and tall RADS), as well as (only for tall RADS) shifted from the symmetry axis by 11 cm along three different directions: along the sun-plane, both *ii)* towards the sun and *iii)* away from the sun, and *iv)* along a plane perpendicular to the sun-plane (sensor is "across" the sun). They all scan in the sun-plane, and within an infinitesimal solid angle $d\Omega$ centered on the viewing-angle θ_s: this was possible owing to the adjoint implementation of the Monte Carlo photon tracking algorithms.

Specific values for the previously described system parameters are given further on in Table 1 (Table 2 provides a set of possible deviations from the standard values).

SIMULATIONS AND PLOTS

The plotted ε_{Ls} is the fundamental simulated quantity: it is the radiance percentage relative error recorded at the RADS sensor, as a function of the viewing-angle θ_s

$$\varepsilon_{Ls} = (L_s - L_{s\text{-RADS}}) / L_s \times 100 ,$$

where $L_{s\text{-RADS}}$ and L_s are the directional radiances, along viewing direction θ_s, in the presence and in the absence, respectively, of the RADS instrument. The viewing-angle θ_s is in the sun-plane, and ranges from 0º (horizontally, towards the sun half-plane) through 90º (vertically down, i.e., at nadir) and up to 180º (horizontally, away from sun). The computed radiances are Monte Carlo unbiased estimators of the expected average responses, precise to within a standard error (standard deviation over mean) of less than 0.01. The correlation existing between perturbed and un-perturbed photon histories allows to obtain even lower standard errors on the estimation of the relative error (Spanier and Gelbard 1969). The former statistical precision has also been obtained by initiating a sufficient number of photons, and by applying adequate variance reduction techniques (Doyle 2000).

In the annexed plots of ε_{Ls} a legend is provided to distinguish between the curves relating to the different sensors. The centrally located sensor for the flat RADS instrument is shadowed according to a directional radiance relative error curve plotted as a thick continuous line, with filled-circle symbols. The central sensor shadowing error for the fully 3D RADS instrument is given with a curve plotted as a thin continuous line, with empty-circle symbols. The towards, away, and across sensors' shadowing curves are plotted as dotted lines, with triangles, dashed lines, with reversed triangles, and dot-dashed lines with square symbols, respectively. Generally, within one plot, five curves are therefore shown, one for a flat disk-like instrument with sensor at center, and four for the 3D RADS instrument: at center, 11 cm towards sun, 11 cm away from sun, and 11 cm "across" sun. The horizontal straight line shows the 10 % error limit, while the dashed vertical line is the in–water antisolar direction.

Simulations, limited to a standard system taken as a reference case for additional Monte Carlo computations obtained by systematically varying one of its parameters at time, are performed and illustrated in this work to investigate the main RADS shadowing features. Table 1 shows the full system parameter set for this particular standard case. Departing from this system, a sensitivity study on the shadowing features can be carried out by varying the parameters as shown in Table 2. Each new case is obtained by varying only one parameter, except for the spectrally varying cases (three wavelengths considered) in which more parameters are simultaneously, but consistently, varied. In Table 2 the parameters defining the standard case are recalled by emphasizing them in bold type, while the three-parameter sets which are spectrally linked to other co-varying sets are put in brackets: these parameters are changed only when changing the incoming wavelength (i.e., they co-vary with λ).

The results of simulations corresponding to the system described in Table 1 are plotted in Fig.1. Fig.1a) shows a logarithmic plot of radiance error versus viewing-angle, Fig.1b) is the linear scaling of the same plot, while Fig.1c) shows details of the region around the shadowing peak. In this standard case considerably distinct features are observed between the flat RADS instrument shadowing curve, and the ones relating to the fully extended 3D RADS instrument. All the simulated curves present a clear and pronounced peak in the surroundings of—but not in exact coincidence with—the

antisolar direction, and the peak falls off in a non-symmetric way w.r.t. this direction. This occurs in a striking way for all but the flat instrument case (in fact a non-symmetric behavior is found also for this case, as more evident in other—not shown here—simulated cases, where the diffuse light regime is stronger).

RESULTS AND DISCUSSION

A detailed description of Fig.1 characteristics will now be undertaken, as it is representative of the main features to be encountered in the shadowing analysis of similar systems. Depending on sun-zenith angle, on diffuse light regime, and on scattering phase function some distinct shadowing effects are more or less pronounced. In what follows we shall call "bumps" the lesser pronounced features which result from the previous combined shadowing effects, and occurring mainly in the lower viewing-angles range.

For the flat RADS instrument, the shadowing curve (—●—) can be subdivided in three main regions where different shadowing effects are at work (after allowance has been made for statistical fluctuations) and in part result from geometry-dependent factors.

1) $\theta_s < 90^\circ$, where a "bumpy" structure reveals a shadowing effect that can be attributed to the in–water scattering phase function characteristics, which are, though, quite convoluted within the overall radiance signal. A basic trend of smooth decrease in shadowing exists from 0 to ~40º (the viewing-angle perpendicular to the refracted antisolar direction) followed by a symmetric increase up to ~80º. This feature is proportional to the smoothly varying viewing-angle optical-path through the directly shadowed water volume: a very sun-position dependent behavior. By simple calculation of the distance the light has to travel in the direct shadow, and by applying beam attenuation to this straight optical path, the resulting shadowing error is slightly over-predicted. This error is in fact decreased somewhat, and with different directional weights, by multiple scattering. The bumps are a result of the phase function, and thus the relative importance of multiple scattering vs single scattering. In a heavily diffuse light regime this structure tends to be swamped by the prevailing uniform shadowing.

2) $\theta_s > 90^\circ$, the direct shadow cast by the instrument is prevailing over any other shadowing feature, and this contribution is quite symmetric w.r.t. the antisolar point for the presently analysed flat disk-like instrument.

3) A superposition exists—over the previous two basic trends—due to the shadowing of downwelling diffuse light. This feature is less sun-position dependent than the others are. This shadow is principally affecting the closer-to-nadir viewing-angles: it is mainly the volume of water sited symmetrically and centrally *under* the RADS instrument that suffers more of RADS blocking such diffuse light. A convex shadowing structure can be seen for viewing directions increasingly lower than ~130º (the antisolar direction in this geometry, which occurs at ~40º more than the vertically down direction), especially from below ~120º, and all the way to ~50º. Within this range, and for the close-to-nadir viewing-angles, the shadowing of diffuse downwelling light is increasingly evident when looking more into the directly illuminated waters, as opposed to directions pointing further towards the direct shadow, where the direct shadowing effect is predominant. On the other hand at viewing angles pointing more into the direct shadow, the diffuse light itself is responsible for filling in the shadow, which is therefore not as deep as expected in single scattering theory.

In considering now the fully 3D cylindrical RADS instrument, the extension in height w.r.t. the flat disk instrument causes some remarkable differences in the resulting shadowing curves. For the centrally located sensor shadowing curve (—O—) two main features can be noted, when compared to the curve for the also centrally located sensor but on the flat RADS instrument: 1) A general but slight increase in shadowing, due to the more intense diffuse shadowing effect, can be appreciated for directions in the range 10–50º. 2) A specific and remarkable increase in shadowing, due to the increased directly shadowed water volume, occurs for directions pointing in the 130–180º range.

For the sensor shifted 11 cm along the sun-plane towards the sun (····Δ····) three main features are worth noting, when compared again to the flat instrument shadowing curve: 1) A decrease in shadowing for directions from 0º to the antisolar direction (~130º), this occurs because the sensor is separated from directly illuminated water by a less extended directly-shadowed water volume. 2) A corresponding increase in shadowing for the remaining directions (~130–180º), for the reason opposite to the one given in the previous point. 3) The shadowing peak is broader and is more clearly shifted to higher viewing directions w.r.t. the exact antisolar direction.

For the sensor shifted 11 cm along the sun-plane, but away from the sun (---∇---), three main features are again to be underlined, and they are generally the opposite counterparts of the previously commented ones, due to the shifted geometry of this case. Worth noting is that this 11 cm-away-from-sun curve is lower for the low viewing-angles, and then is higher for high angles, when compared to its 11 cm-towards-sun counterpart curve.

For the sensor shifted 11 cm perpendicularly to the sun-plane (---❑--), but still scanning radiance in the sun-plane, the following remarks can be made. Intermediate shadowing values, between the two last described cases, are to be found. The shadowing curve is more similar to the centrally located sensor in the fully 3D RADS instrument, but is less intense due to the fact that viewing directions, always along the sun plane, are intersecting the light field perturbation along a smaller cross section through the directly-cast cylinder shadow. Moreover the un-shadowed volume of water is in this case more adjacent to the sensor (this 11 cm-across-sun-plane position is scanning in fact along the edge of directly shadowed waters: there is therefore a confining water region which is flooded by direct sun light, and multiple scattering is more efficient in restoring light).

Finally a comparison has been made, using the standard simulation case presented in this work, between the upwelled radiance L_u shadowing percentage relative error ε_{Lu} as simulated for a 3D RADS instrument with a central sensor, and the one computed using Gordon and Ding's (1992) formulation (which is valid for a flat disk-like instrument). The same has been carried out also for the upwelled irradiance E_u shadowing percentage relative error $\varepsilon_{Eu} = (E_u - E_{u\text{-RADS}}) / E_u \times 100$. Results are shown in Table 3.

This comparison suggests that the conventional shadowing correction scheme seems to underestimate the required shadowing corrections, more so for E_u, compared to when the full 3D instrument height is appropriately simulated. In the case of L_u the difference is not as strong, but the dispersion between shadowing errors amongst sensors that are differently located on the lower face of the instrument may induce a source of error variability that, with full 3D simulations, can be fully accounted for. The extent of these discrepancies will depend on the environmental, geometrical, illumination, and inherent optical properties of the studied system.

CONCLUSIONS

Fully 3D backward Monte Carlo simulations (using the PHOTRACK code) have demonstrated that the anomalous dark zones found in upwelling directional radiance measurements, and especially around the antisolar direction in the RADS instrument, are indeed vestiges of a shadowing effect. This effect has been thoroughly investigated in this work. From the findings a caveat is suggested on the interpretation of data acquired also with other than RADS in–water cylindrical radiometers, even if of the integrating-radiance type (i.e., upwelling irradiance collectors). The extensive shadowing analysis carried out in this work suggests that more refined than current state-of-the-art instrument self-shading correction schemes may be advanced, allowing also for detailed sensor positioning on instrument casing, alignment with respect to sun-position, and fully 3D structure-induced shadowing effects.

As a result from this investigation the rationale for an operational shadow-correction scheme, or of a shadowed-data removal criterion, is provided and can be based, for instance, on real-time PHOTRACK radiative transfer simulations to be applied on individual field data acquisitions performed at sea. This can be operated once the full set of parameters identifying the optical and geometrical characteristics of the specific sun-ocean-atmosphere-RADS system are supplied, as existing at the time of the *in–situ* data acquisition. To provide sensitivity on the predicted shadowing errors, simulations are being completed for a proposed wide range of environmental conditions found at sea, with optical parameters selected to adequately represent some open ocean and coastal areas, in part of their atmospheric and marine variability.

ACKNOWLEDGEMENTS

The authors wish to thank Howard Gordon for his precious advice and comments, and for initially suggesting the topic of this research.

REFERENCES

Buiteveldt, Hakvoort, and Donze, Ocean Optics XIII, Proc. SPIE Int. Soc. Opt. Eng., 225, 174–183, 1994

Doyle and Rief, Math. Comput. Simul., 47, 215–241, 1998

Doyle, PhD Thesis, Imperial College of Science Technology and Medicine, UK, 345, 2000

Frölich and Shaw, Appl. Opt., 19, 1773–1775, 1980

Gordon, Brown, and Jacobs, Appl. Opt., 14, 417–427, 1975

Gordon and Ding, Limnol. Oceanogr., 37, 491–500, 1992

Mobley, Gentili, Gordon, Jin, Kattawar, Morel, Reinersman, Stamnes, and Stavn, Appl. Opt.,32, 7484–, 1993

Morel and Gentili, Appl. Opt., 30, 4427–4438, 1991

Morel and Gentili, Appl. Opt., 32, 6864–6879, 1993

Morel, Voss, and Gentili, J. Geophys. Res., 100, 143–150, 1995

Neckel and Labs, Solar Phys., 90, 205–258, 1984

Petzold, Rep. 510 Ref. 72–78, Scripps Inst. of Oceanogr., 1972

Pope and Fry, Appl. Opt., 36, 8710–8723, 1997

Spanier and Gelbard, Monte Carlo Principles and Neutron Transport Problems, Addison-Wesley, 234, 1969
Sturm and Zibordi, Int. J. Remote Sens., submitted, 2000
Vigroux, Ann. Phys., Ann. Phys., 8, 709–762, 1953
Voss, Opt. Eng., 28, 241–247, 1989
Young, Appl. Opt., 19, 3427–3428, 1980

Table 1: System parameters for the standard reference case.

Sun:	point light source at infinity
λ	555 nm
E_0	1.902 W m^{-2} sr^{-1}
θ_0	60º
Atmosphere:	one homogeneous layer, 60 km deep
n_{atm}	1.000
ozone load	350 DU [$\tau_{ozo}(555) = 0.0332$]
atm. pressure	1013.25 hPa [$\tau_{mol}(555) = 0.0936$]
τ_{aer}	0.05
$phfn_{aer}$	TTHG 1, the two-term Henyey-Greenstein function (#1) computed, at 555 nm, from sun photometer measurements carried out at a North Adriatic oceanographic tower site, averaged over a historical data set (Sturm and Zibordi 2000) with function coefficients given by $g_1 = 0.623$, $g_2 = 0.473$, $as = 0.960$.
air-sea interface	flat
Ocean:	one homogeneous layer, infinitely deep
n_{oce}	1.341
a_w	Pope and Fry (1997) (P&F) [a_w (555) = 0.0596 m^{-1}]
b_w	Buiteveldt et al (1994) (Bu) [b_w (555) = 0.0014 m^{-1}]
a_p	0.01 m^{-1}
b_p	0.09 m^{-1}
c_p	0.10 m^{-1}
ω_{0p}	0.9
$phfn_p$	Gordon's KA (Gordon, Brown and Jacobs 1975)
RADS casing:	black cylinder (or disk): 20 cm radius, 50 cm tall (or ~0 cm tall)
sensors depth	-1.00 m
sensors n.	4+1
sensors location	one on 3D RADS symmetry axis, and three at 11 cm from it: one towards, and one away, from the sun-point along the sun-plane, and one across it. One further case is for a flat RADS-like instrument (i.e., a disk) with the sensor at center of disk. All sensors are located on lower circular face of instrument, and looking down.
sensors $d\Omega$	infinitesimally thin solid angle, centered around viewing-angle θ_s
view angles n.	21, scanning along the sun-plane (every 10º—plus a few at specific intermediate angles—looking at upwelled directions), for each sensor. (8 extra angles to resolve, in one case, the shadowing peak details).
simulated quant.	percentage relative error on shadowed in–water directional radiance: $\varepsilon_{Ls} = (L_s - L_{s\text{-RADS}}) / L_s \times 100$, where L_s and $L_{s\text{-RADS}}$ are the sun-plane directional radiances, along viewing direction θ_s, in the presence and in the absence, respectively, of the RADS instrument.

Table 2: Variations of system parameters for the proposed sensitivity study cases.

Sun:	no change
λ	[443; **555**; 665 nm]
E_0	[1.950; **1.902**; 1.564 W m^{-2} sr^{-1}]
θ_0	0, 15, 30, 45, **60**, 75º
Atmosphere:	no structural change, one case is with no atmosphere (i.e., black sky)
n_{atm}	no change
ozone load	no change (350 DU) [τ_{ozo}(443; **555**; 665) = 0.0010; **0.0332**; 0.0182]
atm. pressure	no change (1013 hPa) [τ_{mol}(443; **555**; 665) = 0.2359; **0.0936**; 0.0449]
τ_{aer}	no-atmosphere, 0.00, **0.05**, 0.30, 1.00, overcast (isotropic sky-light)
phfn$_{aer}$	[TTHG$_{443}$ 1; TTHG$_{\mathbf{555}}$ **1**; TTHG$_{665}$ 1], TTHG 2, TTHG 3 [g_1=0.623,**0.623**,0.623; g_2=0.513,**0.473**,0.434; as=0.975,**0.960**,0.945]. TTHG **1: g_1 = 0.623, g_2 = 0.473, as = 0.960** TTHG 2: g_1 = 0.820, g_2 = 0.550, as = 0.980 TTHG 3: g_1 = 0.950, g_2 = 0.000, as = 1.000 (single term HG function)
air-sea interface	no change
Ocean:	no structural change
n_{oce}	no change
a_w	no change (P&F) [a_w(443, **555**, 665)=0.00707, **0.0596**, 0.4290m^{-1}]
b_w	no change (Bu) [b_w(443, **555**, 665)=0.00348, **0.0014**, 0.0006m^{-1}]
a_p	as from combinations of c_p and ω_{0p} below: $a_p = (1 - \omega_{0p})\, c_p$
b_p	as from combinations of c_p and ω_{0p} below: $b_p = \omega_{0p} c_p$
c_p	0.03, **0.10**, 0.30, 1.0 m^{-1}
ω_{0p}	0.5, 0.8, **0.9**
phfn$_p$	Gordon's KC, Gordon's **KA** (Gordon et al 1975), Petzold (1972)*
RADS casing:	no change
sensors depth	0$^-$ (only for flat RADS), **-1.00**, -3.00, -5.00, -10.0, -30.0 m
sensors n.	no change
sensors location	no change
sensors $d\Omega$	no change
view angles n.	no change
simulated quant.	no change

*: as tabulated by Mobley et al (1993). Note: standard case parameters are in bold type.

Table 3: RADS self-shadowing percentage relative errors compared with Gordon and Ding (1992) formulations, both for L_u and E_u.

[%]	ε	ε (sun)	ε (sky)	r	ε^{GD}	$(\varepsilon - \varepsilon^{GD}) / \varepsilon \times 100$
L_u	***4.541***	3.889	6.216	0.1971	***4.273***	**5.9**
E_u	***4.415***	3.379	”	”	***3.848***	**12.8**

ε is the shadowing percentage relative error computed with PHOTRACK, ε (sun) and ε (sky) are the errors due solely from the sun and sky, respectively (Gordon and Ding 1992), r is the ratio of diffuse to direct above-surface irradiance as computed by the PHOTRACK code, and ε^{GD} is the shadowing percentage relative error from Gordon and Ding's formulation. The last column shows the relative error between the two determinations. Errors are assessed for the reference system described in Table 1 (with total in–water absorption coefficient $a_t \approx 0.07$ m^{-1} and instrument radius R = 20 cm; if R = 5 cm the same ε^{GD} would have been obtained for $a_t \approx 0.27$ m^{-1}).

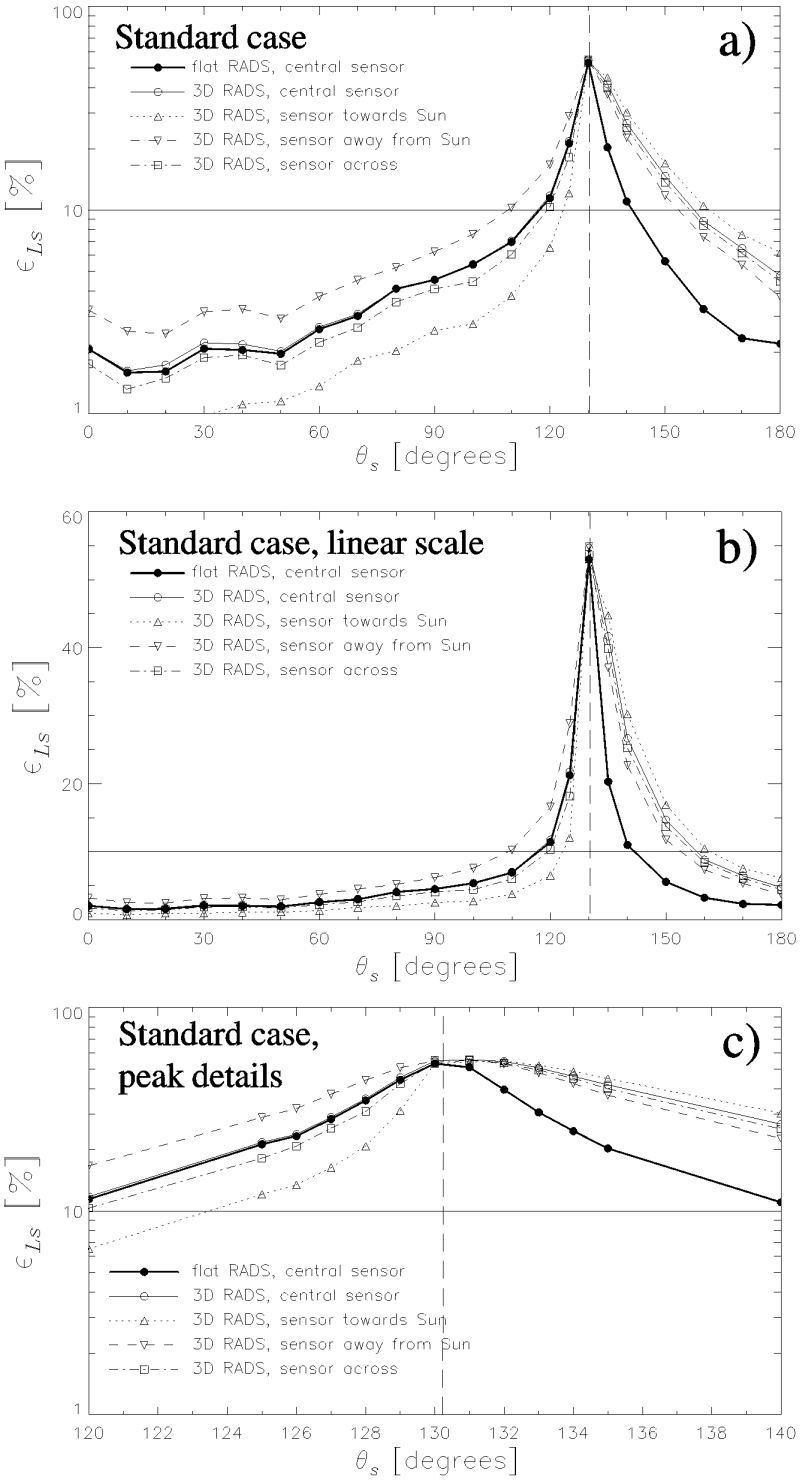

Fig. 1: The standard case, defining initial conditions for the simulations: λ=555nm, θ_0 =60deg, τ_{ozo} =0.0332, τ_{mol} =0.0936, τ_{aer} =0.05, phfn$_{aer}$ =THGG 1, n_{atm} =1.000, n_{oce} =1.341, flat air-sea interface, 60km atm. layer, inf. deep ocean layer, a_w =0.0596m^{-1}, b_w =0.0014m^{-1}, a_p =0.0100m^{-1}, b_p =0.0900m^{-1}, phfn$_p$ =Gordon KA, RADS casing is totally absorbing, RADS sensors depth=1.00m. Plotted $\varepsilon_{Ls} = (L_s\text{-}L_{s\text{-RADS}}) / L_s$*100 is the radiance percentage error measured at RADS sensor within an infinitesinal solid angle, as a function of sensor viewing angle θ_s , and scanning in the solar plane. Viewing angle θ_s ranges from 0° (horizontally towards sun) through 90° (down) and up to 180° (horizontally away from sun). The towards (dots), away (dashes), and across (dot-dash) sensors are located 11cm from the RADS cylinder axis. The central (thick line: flat RADS, thin line: extended 3D RADS) sensors are on-axis. Horizontal line is the 10% error limit, dashed vertical line is the in-water anti-solar direction.